

Revealing the role of crystal orientation of protective layers for stable zinc anode

Qi Zhang¹, Jingyi Luan¹, Xiaobing Huang², Qi Wang¹, Dan Sun¹, Yougen Tang¹, Xiaobo Ji¹ & Haiyan Wang¹  [✉]

Rechargeable aqueous zinc-ion batteries are a promising candidate for next-generation energy storage devices. However, their practical application is limited by the severe safety issue caused by uncontrollable dendrite growth on zinc anodes. Here we develop faceted titanium dioxide with relatively low zinc affinity, which can restrict dendrite formation and homogenize zinc deposition when served as the protective layer on zinc anodes. The as-prepared zinc anodes can be stripped and plated steadily for more than 460 h with low voltage hysteresis and flat voltage plateau in symmetric cells. This work reveals the key role of crystal orientation in zinc affinity and its internal mechanism is suitable for various crystal materials applied in the surface modification of other metal anodes such as lithium and sodium.

¹Hunan Provincial Key Laboratory of Chemical Power Sources, College of Chemistry and Chemical Engineering, Central South University, Changsha 410083, P. R. China. ²College of Chemistry and Chemical Engineering, Hunan University of Arts and Science, Changde 415000, P. R. China. ✉email: wanghy419@csu.edu.cn

Achieving higher energy density is the main development tendency for the next-generation battery system¹. Metal anodes, such as lithium (Li), sodium (Na), and zinc (Zn), with high theoretical capacity and low electrochemical potential are considered as the most promising materials to meet this requirement^{2,3}. However, the electrochemical performance of metal anodes is seriously affected by the dendrite formation during repeated charging and discharging. Metal dendrites are easily detached from anode mainbody and the newly exposed metal would react with electrolyte, leading to low Coulombic efficiency^{4,5}. More seriously, separators may be punctured by the continuous dendrite growth, which directly causes the short circuit and poor cycle life of batteries^{6,7}. Therefore, it is important to solve this issue for the industrialization of metal anodes.

Many approaches have been developed to achieve safer metal anodes, which mainly focus on two aspects: (1) improving metal deposition on current collectors. Nucleation can be facilitated by a three-dimensional structure with a uniform local electric field^{8,9}. Some metal-affinity modification layers induced on current collectors are conducive to the adsorption of metal ions, which can guide the deposition and further alleviate dendrites^{10–12}. (2) Optimizing the interface between metal and electrolyte. An artificial solid electrolyte interface (SEI) or an additional layer with inferior metal affinity can be applied as a protective layer to restrict dendrite growth^{13,14}. Metal affinity is a key criterion to judge the applicable functions (guiding or restricting). However, taking titanium dioxide (TiO₂) for example, it can be used both for modification of current collectors and protection of metal anodes according to previous reports^{15–17}. These results seem contradictory because good metal affinity is required when TiO₂ is used as a decoration on current collectors to homogenize metal deposition while low metal affinity is necessary if it is served as a protective layer^{18,19}. TiO₂ can be simultaneously applied to two different metal modification strategies with opposite requirements, indicating that there is an ambiguous internal mechanism affecting its metal affinity. Considering that exposed facets of a crystal have a great influence on catalytic activity, metal affinity may be also controllable by adjusting surface exposure^{20,21}.

In this work, the interactions between Zn and different facets of TiO₂ are first investigated by density functional theory (DFT) calculation and it is concluded that the (0 0 1) and (1 0 1) facets of TiO₂ show relatively low Zn affinity. Accordingly, TiO₂ with highly exposed (0 0 1) facet is prepared and applied as the protective layer for Zn metal anodes. The (0 0 1) faceted TiO₂ layer can effectively prevent Zn dendrites from growing vertically and stabilize the interface between anode and electrolyte. As a result, the modified Zn anode exhibits long-term cycle life during Zn stripping and plating.

Results

Theoretical analysis and characterization of faceted TiO₂. The mechanism for the interaction between Zn and different facets of TiO₂ is first investigated by DFT calculation. As shown in Fig. 1a–c and Supplementary Figs. 1 and 2, the models of Zn atoms attached to TiO₂ surfaces and Zn surfaces were constructed. The Zn affinity of TiO₂ surfaces can be judged by comparing the binding energy of Zn atom attached to the TiO₂ surface and Zn surface. It can be considered that a TiO₂ facet is with high Zn affinity if the binding energy of Zn atom attached to the corresponding TiO₂ facet is higher than that on the Zn surface. As summarized in Fig. 1d, the binding energy between Zn atom and TiO₂ (1 0 0) facet is -0.95 eV, higher than that between Zn atom and Zn surfaces (-0.68 and -0.86 eV), indicating that Zn prefers to deposit on TiO₂ (1 0 0) facet in comparison to Zn surface. It is detrimental for a protective layer since this priority

can lead to the growth of Zn dendrites upon the layer and deactivate the protective effect. In contrast, there is a weaker absorption of Zn on TiO₂ (0 0 1) and (1 0 1) facets with the binding energy of -0.63 and -0.45 eV, respectively, which is mainly because the more exposure of the lower coordinated Ti on these facets exhibits more intense repulsion to Zn atom²². The interaction between Zn and different TiO₂ facets is illustrated in Fig. 1e. According to the above analysis, the facet orientation plays a key role in Zn affinity and suitable materials for a protective layer can be achieved by controlling the exposure of specific facet.

As shown in Fig. 1f, the X-ray diffraction (XRD) patterns of the as-prepared faceted TiO₂ (F-TiO₂) and commercial TiO₂ (C-TiO₂) can be indexed to anatase TiO₂. The average thickness along the growth direction of a crystal (D) can be calculated by Scherrer equation^{23,24}:

$$D = \frac{K\lambda}{\beta \cos\theta} \quad (1)$$

where K , λ , β , and θ represent Scherrer constant, the wavelength of X-ray, full width at half maximum (FWHM) of diffraction peak and Bragg angle, respectively. For a specific crystal orientation, the larger FWHM in the XRD pattern indicates the smaller D in this direction, in other words, the larger exposed area of the corresponding facet (Supplementary Fig. 3)²⁵. Accordingly, the broader (0 0 4) peak in F-TiO₂ demonstrates the larger exposure of (0 0 1) facet and the narrower (2 0 0) peak F-TiO₂ corresponds to the larger crystal size parallel to (0 0 1) facet, which is also the evidence of the relatively higher exposed area of (0 0 1) facet in comparison with C-TiO₂²⁶. In Raman spectra (Supplementary Fig. 4), the characteristic peaks of anatase TiO₂ appear at 392.3 cm⁻¹ (symmetric bending vibration, B_{1g}), 513.7 cm⁻¹ (antisymmetric bending vibration, A_{1g}), 636.5 cm⁻¹ (symmetric stretching vibration, E_g)²⁷. The 3-coordinated titanium (Ti) atoms on the (0 0 1) surface (Supplementary Fig. 5a) with lower coordination number than the 5-coordinated Ti atoms on (1 0 0) surface (Supplementary Fig. 5b) tend to show stronger bending vibration²⁸. Therefore, the weaker A_{1g} and B_{1g} peaks in the Raman spectrum of F-TiO₂ suggest its higher exposure of (0 0 1) facet. Transmission electron microscopy (TEM) images (Supplementary Fig. 6) clearly show the nanosheet structure of F-TiO₂ with average width and thickness of 50 and 5 nm, respectively. From the side view of F-TiO₂ nanosheet (Fig. 1g), lattice fringes with a lattice spacing of 0.235 nm are observed, which demonstrates that the [0 0 1] direction is perpendicular to the top surface. Figure 2h is the top-view high-resolution transmission electron microscopy (HRTEM) image of F-TiO₂ nanosheet. There are orthogonal lattice fringes with equal lattice spacing (0.19 nm) inside the nanosheet (Fig. 1i), corresponding to [1 0 0] and [0 1 0] directions (both belong to <1 0 0> family of directions). Therefore, the normal direction of top surface is [0 0 1] direction perpendicular to both [1 0 0] and [0 1 0] directions²⁹. According to the observation of side-view and top-view HRTEM images, it is confirmed that (0 0 1) facet is the highly exposed top surface of F-TiO₂ nanosheet. Another set of orthogonal lattice fringes corresponding to [1 0 1] and [0 1 0] directions (Fig. 1j) indicates the existence of (1 0 -1) or (-1 0 1) facets (equivalent to (1 0 1) facet because of the tetragonal symmetry) at the edge of nanosheet³⁰. Besides, the side surface intersects the top (0 0 1) surface at an obtuse angle (Fig. 1g and Supplementary Fig. 6c). It can be concluded that the side surface of F-TiO₂ nanosheet is (1 0 1) facet rather than the vertical (1 0 0) facet. The percentage of the exposed (0 0 1) and (1 0 1) facets can be calculated to be 83% and 17%, respectively, by considering the nanosheet as a compressed square frustum. With regard to C-TiO₂ (Supplementary Fig. 7), it exhibits a nanoparticle morphology with an

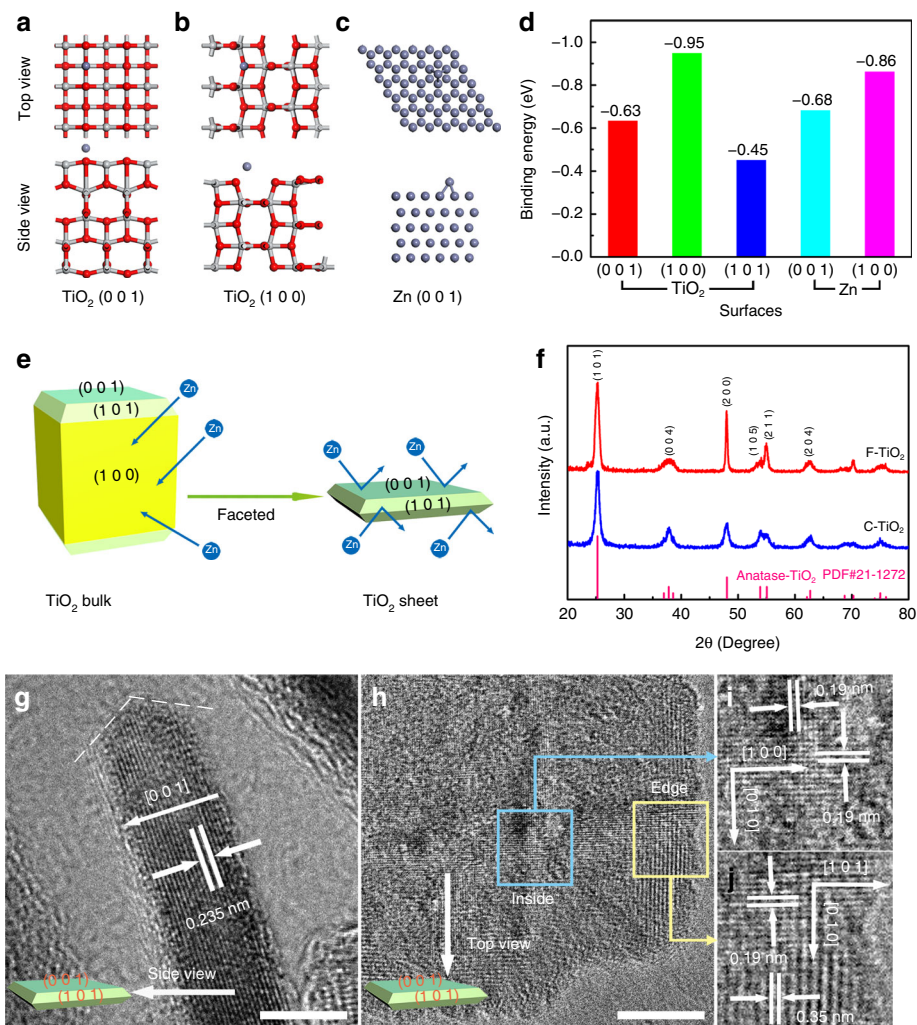


Fig. 1 Theoretical simulation and characterization of F- TiO_2 . Calculations models of Zn absorbed on **a** TiO_2 (0 0 1) facet, **b** TiO_2 (1 0 0) facet, and **c** Zn (0 0 1) facet. **d** Calculated binding energies of Zn atom with different facets. **e** Schematic illustration of the interaction between Zn and anatase TiO_2 with different exposed facets. **f** XRD patterns of F- TiO_2 and C- TiO_2 . **g-j** HRTEM images of F- TiO_2 . Scale bars: 5 nm.

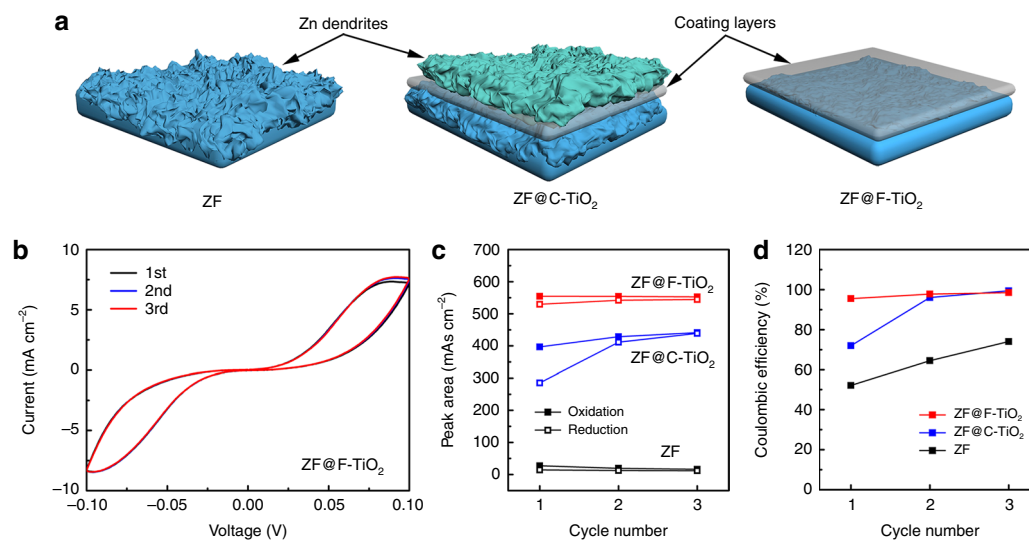


Fig. 2 Zn deposition behavior of the prepared anodes. **a** Schematic illustration of the Zn plating process with different coating layers. **b** CV curves of Zn-Zn symmetric cells using ZF@F- TiO_2 anode measured at 1 mV s^{-1} . Peak areas of Zn stripping/plating reactions (**c**) and corresponding Coulombic efficiency (**d**) of the prepared Zn anodes in Zn-Zn symmetric cells.

average diameter of 20 nm and the irregular lattice fringes indicate its random growth orientation, which leads to more exposure of TiO₂ (1 0 0) facets. The large area of extra TiO₂ (1 0 0) facet is detrimental to prevent the growth of Zn dendrites. Accordingly, it is believed that F-TiO₂ nanosheets with exposed (0 0 1) and (1 0 1) facets can completely shield Zn and restrict the formation of dendrites.

Electrochemical performance of F-TiO₂ as a protective layer.

TiO₂ protective layer was introduced on Zn anode by a simple blade coating method and the corresponding XRD pattern (Supplementary Fig. 8) demonstrates that the composite Zn anode is successfully synthesized. The Zn plating process on different Zn anodes is illustrated in Fig. 2a. Charges and ions tend to accumulate on the small tips at the surface of commercial Zn foil anodes when there is an impressed voltage. The resulting uneven interfacial electric field and ion concentration can induce preferential Zn growth and eventually lead to the formation of Zn dendrites during the repeated stripping and plating cycles³¹. When using C-TiO₂ as the intermediate layer, Zn tends to grow on the surface of TiO₂ layer with a higher Zn affinity. For comparison, the Zn plating reaction can be well confined under the protective layer and the smooth Zn layer can be deposited on the Zn anode by faceting the TiO₂ to specific orientations with low Zn affinity. The cyclic voltammetry (CV) curves of F-TiO₂ coated Zn foil (ZF@F-TiO₂) in Zn-Zn symmetric cells (Fig. 2b) can almost maintain the identical shapes in comparison with the changed peaks of C-TiO₂ coated Zn foil (ZF@C-TiO₂) and Zn foil (ZF) (Supplementary Fig. 9), which indicates the superior reversibility of Zn stripping/plating in ZF@F-TiO₂ anode. The peak areas of each redox reaction of CV curves can be obtained by integration operation (Fig. 2c). The larger peak area of ZF@F-TiO₂ anode reflects the enhanced interfacial activity for Zn deposition³². Zn²⁺ driven by the electric field and concentration gradient migrate toward the Zn anode and tend to be repulsed by the F-TiO₂ layer at the interface, leading to the Zn²⁺ accumulation near the anode surface. The increased Zn²⁺ concentration can not only activate more binding sites for Zn deposition but also accelerate the Zn²⁺ transfer rate on the surface to alleviate the uneven Zn²⁺ distribution, which is beneficial to the ordered interfacial Zn deposition^{33,34}. Moreover, the highest Coulombic efficiency (reduction/oxidation) of ZF@F-TiO₂ among all the prepared anodes (Fig. 2d) is also the evidence of its superior reversibility, which can be ascribed to the more uniform Zn deposition and less formation of “dead Zn”. TiO₂ coated Zn foils exhibit better hydrophilicity than pure Zn foil (Supplementary Fig. 10), indicating that electrolyte can penetrate TiO₂ layers to facilitate Zn²⁺ transport towards anode surface. The voltage profiles of the first ten cycles of zinc-stainless steel (Zn-SS) cells were recorded, which are shown in Supplementary Fig. 11. Pure Zn foil fails rapidly within 600 min due to the short circuit caused by the formation of dendrites. And the cycling stability of the cells is significantly improved when Zn foils are coated with the TiO₂ interface layer. Specifically, ZF@F-TiO₂ exhibits longer cycling life than ZF@C-TiO₂, indicating its better Zn reversibility achieved by the specific exposed facets.

Zn anodes were extracted from Zn-SS cells and their digital photographs are shown in Supplementary Fig. 12. Some unevenly distributed crystals are formed on the surface of ZF and ZF@C-TiO₂, while ZF@F-TiO₂ can maintain the original structure of F-TiO₂ layer. Scanning electron microscope (SEM) images of these cycled electrodes were also compared with the fresh anodes (Fig. 3). The morphologies of ZF@F-TiO₂ and ZF@C-TiO₂ are consistent before cycling. TiO₂ coating layer with a smooth surface and uniform thickness (20 μm) is in close contact with Zn

foil. After cycling, there is no obvious change in ZF@F-TiO₂ and its interface is still tightly combined. The well-defined distribution of Ti and Zn in the energy dispersive X-ray (EDX) mapping images (Fig. 3c, f) also demonstrates the good reversibility during stripping and plating cycles. As shown in Fig. 3j, k, Zn sheets (3 μm in length) are observed on the surface of cycled ZF@C-TiO₂, which is easily turned into Zn dendrites and causes the safety problem. C-TiO₂ layer seems ineffective due to a large amount of Zn transferred from Zn foil and the formation of void space at the interface. The process of Zn transfer to the surface can be seen in the EDX mapping image (Fig. 3l). Supplementary Fig. 13 exhibits the more disordered surface with the wild growth of Zn dendrites on the cycled pure Zn foil, which is in agreement with the short-circuited Zn-SS cell within 10 cycles. From the different morphologies mentioned above, it is proved that the facet orientation plays an important role in adjusting Zn deposition behavior and TiO₂ protective layer with highly exposed (0 0 1) facet with low Zn affinity can completely confine the Zn deposition in the restricted space. Besides, the TiO₂ layer on the cycled anodes was removed by using methyl-2-pyrrolidinone (NMP) to dissolve polyvinylidene difluoride (PVDF) in the layers. As seen from the SEM images of the Zn surface after cycling (Supplementary Fig. 14), Zn deposition in ZF@F-TiO₂ is flat and tends to accumulate parallel to the Zn surface, which also suggests the limited Zn growth by F-TiO₂ protective layer with decreased Zn affinity.

The positive effect of the F-TiO₂ layer on Zn plating behavior was further investigated by testing the cycling stability of Zn anodes in Zn/Zn symmetric cells. As shown in Fig. 4a, ZF@F-TiO₂ can be operated steadily for more than 460 h at 1 mA cm⁻² for 1 mAh cm⁻², which is much superior to ZF@C-TiO₂ (190 h) and ZF (20 h). When increasing the current density to 2 mA cm⁻² and the specific capacity to 2 mAh cm⁻² (Fig. 4b), ZF@F-TiO₂ can still charge and discharge for 280 h in contrast to the quick failure of ZF@C-TiO₂ and ZF with the shorter lifespan of 115 and 15 h, respectively. Besides, ZF@F-TiO₂ exhibits the most stable voltage plateau and the lowest voltage hysteresis, reflecting the enhanced Zn transfer kinetics³⁵. The electrochemical performance of ZF@F-TiO₂ is competitive in comparison with several Zn anodes using protective coating materials (Supplementary Table 1). The full cells were assembled with the as-prepared Zn anodes and commercial manganese dioxide (MnO₂) cathode. The full cell using ZF@C-TiO₂ anode exhibits the lowest polarization voltage and best cycling performance with the capacity retention ratio of 84.1% after 300 cycles (Supplementary Fig. 15). The enhanced full cell performance using the F-TiO₂ layer suggests its potential for practical application.

Discussion

High-performance Zn anode without external dendrite growth was fabricated by coating TiO₂ with highly exposed (0 0 1) facet on commercial Zn foil. Benefiting from the specific crystal orientation of TiO₂ with abomination to Zn absorption, Zn²⁺ transferred by the electric field was enriched on the anode surface. Thus, the increased interfacial Zn²⁺ concentration could induce uniform nucleation and the further Zn deposition was guided to grow laterally. The as-prepared Zn anode exhibited superior Zn stripping and plating performance with a long lifespan (460 h at 1 mA cm⁻² for 1 mAh cm⁻²). More importantly, the strategy to change the Zn affinity by adjusting the exposure of the facet provides a deep insight into the internal mechanism of metal affinity and can be extended to interfacial modification for other metal anodes.

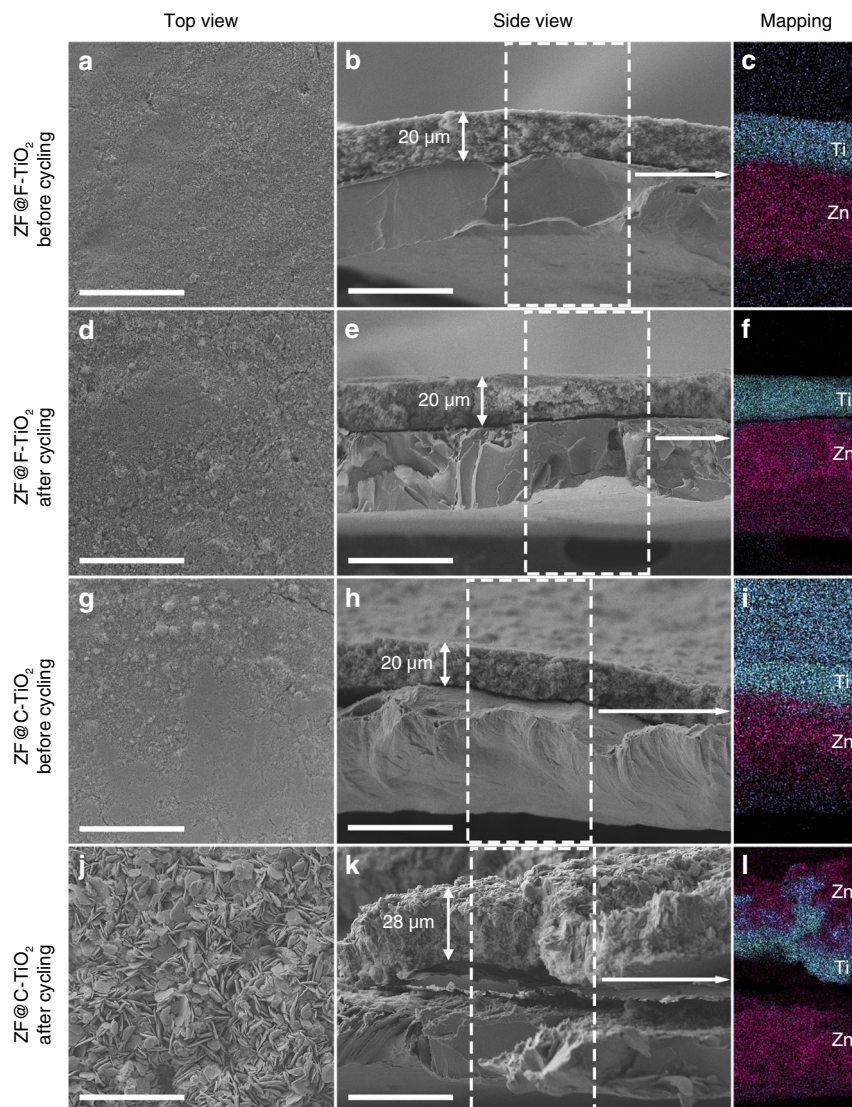


Fig. 3 Morphology evolution of the prepared Zn anodes. SEM and the corresponding EDX mapping images of **a–f** ZF@F-TiO₂ and **g–l** ZF@C-TiO₂ before and after 10 cycles in Zn-SS cells. Scale bar: 40 μm.

Methods

Synthesis of F-TiO₂. Tetrabutyl titanate (10 mL, Aladdin) and hydrofluoric acid (1.2 mL, 40 wt%, Sinopharm) were added into a 50 mL Teflon-lined autoclave and then maintained at 180 °C for 24 h. The precipitates were collected by vacuum filtration then washed by ethanol and dried at 80 °C for 6 h.

Fabrication of ZF@F-TiO₂. F-TiO₂ and PVDF were mixed in a weight ratio of 9:1 with NMP as the dispersant. The slurry was pasted onto Zn foil (30 μm) and dried at 80 °C for 24 h under vacuum. For comparison, ZF@C-TiO₂ was also prepared by replacing F-TiO₂ with C-TiO₂.

Characterizations. XRD was tested by a Bruker D8 X-ray diffractometer with monochromatized Cu Kα radiation (wavelength = 1.5406 Å). Raman spectra were recorded using a Renishaw inVia spectrometer using an excitation wavelength of 532 nm. Morphologies of the prepared TiO₂ and Zn anodes were characterized by SEM (Nova NanoSEM 230) and TEM (Tecnai G2 F20 S-TWIN). The contact angle was measured by a drop shape analyzer (DSA100).

Electrochemical measurements. Coin-type cells (CR2025) were assembled for Zn–Zn symmetric cells, Zn–SS half cells and Zn–MnO₂ full cells with glass fiber as separator and 1 M zinc sulfate (ZnSO₄) aqueous solution as the electrolyte. Battery performance was evaluated using a Neware battery testing system. CV measurement for Zn–Zn symmetric cells was conducted on a CHI760E electrochemical workstation in the voltage range of –0.1–0.1 V. Zn–SS half cells were cycled with a

specific capacity of 1 mAh cm^{–2} at 1 mA cm^{–2} for the charging process and a cut-off potential of –0.3 V at 1 mA cm^{–2} for the discharging process. Full cells were cycled between 1.0 and 2.0 V using commercial MnO₂ (Macklin) as the cathode. In all, 0.1 M manganese sulfate (MnSO₄) was added in the ZnSO₄ electrolyte to prevent Mn²⁺ dissolution.

Computational details. The first-principles calculations were conducted using generalized gradient approximation (GGA) and Perdew–Burke–Ernzerhof (PBE) exchange–correlation functional in DMol3 module of Materials Studio (version 8.0) of Accelrys Inc. An all-electron numerical basis set with polarization functions (DNP basis set) and a DFT–D method within the Grimme scheme was employed. The convergence tolerance was set to 1.0 × 10^{–5} Ha (1 Ha = 27.21 eV) for energy, 2.0 × 10^{–3} Ha Å^{–1} for maximum force and 5.0 × 10^{–3} Å for maximum displacement. Common facets of TiO₂ and Zn were investigated in this simulation, including TiO₂ (0 0 1), TiO₂ (1 0 0), TiO₂ (1 0 1), Zn (0 0 1) and Zn (1 0 0). Each facet was set as a five-layer 3 × 3 supercell with top three-layer atoms releasable. Zn atom was placed in the vertex of the oxygen octahedron of the TiO₂ facet or the tetrahedral vertex of the Zn facet before geometry optimization. Binding energy (E_b) was calculated by the following equation:

$$E_b = E_{\text{total}} - E_{\text{sub}} - E_{\text{Zn}} \quad (2)$$

E_{total} , E_{sub} , and E_{Zn} represent the total energy of the facet combined with Zn atom, the energy of the facet and the energy of Zn atom, respectively.

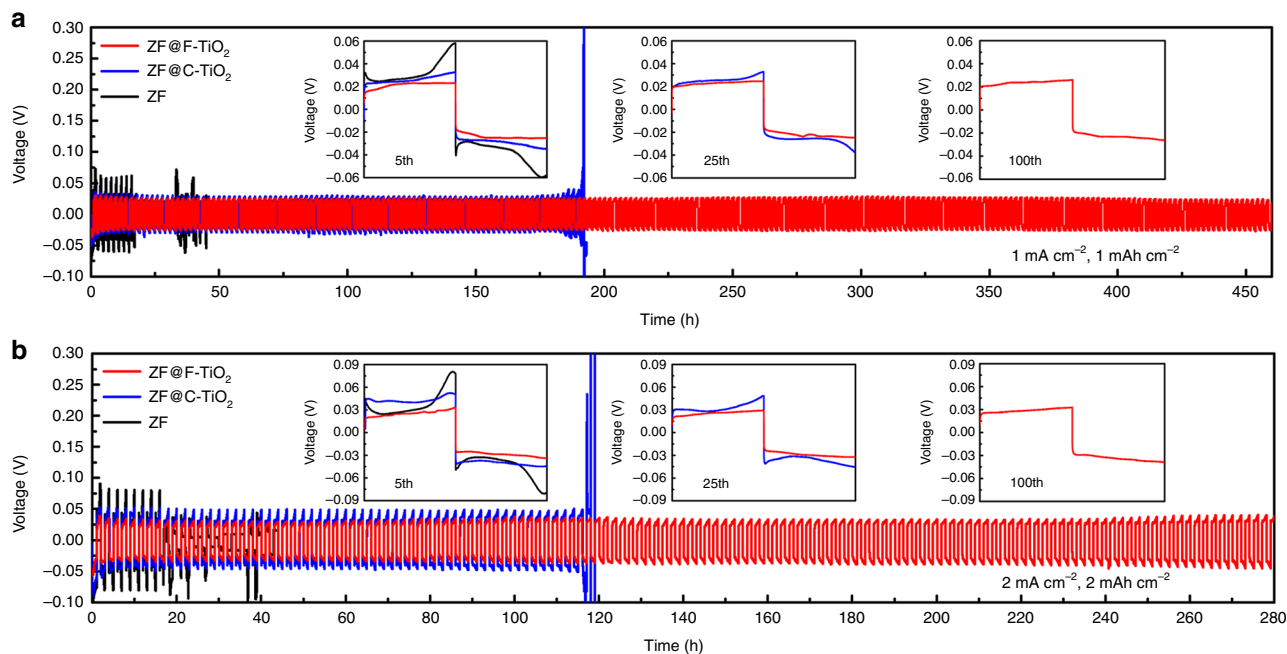


Fig. 4 Electrochemical performance of prepared Zn anodes. Cycling performance Zn-Zn symmetric cells at **a** 1 mA cm^{-2} for 1 mAh cm^{-2} and **b** 2 mA cm^{-2} for 2 mAh cm^{-2} .

Data availability

The data sets generated and/or analyzed in this study are available from the corresponding author on reasonable request.

Received: 24 November 2019; Accepted: 2 July 2020;

Published online: 07 August 2020

References

- Lee, B., Paek, E., Mitlin, D. & Lee, S. W. Sodium metal anodes: emerging solutions to dendrite growth. *Chem. Rev.* **119**, 5416–5460 (2019).
- Lu, Z. et al. Graphitic carbon nitride induced micro-electric field for dendrite-free lithium metal anodes. *Adv. Energy Mater.* **9**, 1803186 (2019).
- Grey, C. P. & Tarascon, J. M. Sustainability and in situ monitoring in battery development. *Nat. Mater.* **16**, 45 (2016).
- Shen, X. et al. Lithium anode stable in air for low-cost fabrication of a dendrite-free lithium battery. *Nat. Commun.* **10**, 900 (2019).
- Meng, J., Chu, F., Hu, J. & Li, C. Liquid polydimethylsiloxane grafting to enable dendrite-free Li plating for highly reversible Li-metal batteries. *Adv. Funct. Mater.* **29**, 1902220 (2019).
- Wu, J. et al. Ultralight layer-by-layer self-assembled MoS_2 -polymer modified separator for simultaneously trapping polysulfides and suppressing lithium dendrites. *Adv. Energy Mater.* **8**, 1802430 (2018).
- Zhang, Q. et al. The Three-dimensional dendrite-free zinc anode on a copper mesh with a zinc-oriented polyacrylamide electrolyte additive. *Angew. Chem. Int. Ed.* **58**, 2–9 (2019).
- Yang, C. P., Yin, Y. X., Zhang, S. F., Li, N. W. & Guo, Y. G. Accommodating lithium into 3D current collectors with a submicron skeleton towards long-life lithium metal anodes. *Nat. Commun.* **6**, 8058 (2015).
- Zeng, Y., et al. Dendrite-free zinc deposition induced by multifunctional CNT frameworks for stable flexible Zn-ion batteries. *Adv. Mater.* **31**, 1903675 (2019).
- Chen, X. et al. Lithiophilicity chemistry of heteroatom-doped carbon to guide uniform lithium nucleation in lithium metal anodes. *Sci. Adv.* **5**, eaau7728 (2019).
- Zhang, Q., Luan, J., Sun, D., Tang, Y. & Wang, H. Plasma-treated Ti^{3+} -doped sodium titanate nanosheet arrays on titanium foil as a lithiophilic current collector for a stable lithium metal anode. *Chem. Commun.* **55**, 6551–6554 (2019).
- Luan, J. et al. Plasma-strengthened lithiophilicity of copper oxide nanosheet-decorated Cu foil for stable lithium metal anode. *Adv. Sci.* **6**, 1901433 (2019).
- Liu, F. et al. Fabrication of hybrid silicate coatings by a simple vapor deposition method for lithium metal anodes. *Adv. Energy Mater.* **8**, 1701744 (2018).
- Deng, K. et al. Single-ion conducting artificial solid electrolyte interphase layers for dendrite-free and highly stable lithium metal anodes. *J. Mater. Chem. A* **7**, 13113–13119 (2019).
- Xue, P., Sun, C., Li, H., Liang, J., & Lai, C. Superlithiophilic amorphous SiO_2 - TiO_2 distributed into porous carbon skeleton enabling uniform lithium deposition for stable lithium metal batteries. *Adv. Sci.* **6**, 1900943 (2019).
- Zhou, M., Lyu, Y., Liu, Y. & Guo, B. Porous scaffold of TiO_2 for dendrite-free lithium metal anode. *J. Alloy. Compd.* **791**, 364–370 (2019).
- Nan, Y., Li, S., Li, B. & Yang, S. An artificial TiO_2 /lithium n-butoxide hybrid SEI layer with facilitated lithium-ion transportation ability for stable lithium anodes. *Nanoscale* **11**, 2194–2201 (2019).
- Zhao, Z. et al. Long-life and deeply rechargeable aqueous Zn anodes enabled by a multifunctional brightener-inspired interphase. *Energy Environ. Sci.* **12**, 1938–1949 (2019).
- Bai, M. et al. A scalable approach to dendrite-free lithium anodes via spontaneous reduction of spray-coated graphene oxide layers. *Adv. Mater.* **30**, 1801213 (2018).
- Li, C. et al. Facet-dependent photoelectrochemical performance of TiO_2 nanostructures: an experimental and computational study. *J. Am. Chem. Soc.* **137**, 1520–1529 (2015).
- Wang, S., Liu, G. & Wang, L. Crystal facet engineering of photoelectrodes for photoelectrochemical water splitting. *Chem. Rev.* **119**, 5192–5247 (2019).
- Liu, G. et al. Enhanced photoactivity of oxygen-deficient anatase TiO_2 sheets with dominant {001} facets. *J. Phys. Chem. C* **113**, 21784–21788 (2009).
- D'Agostino, A. Determination of thin metal film thickness by X-ray diffractometry using the Scherrer equation, atomic absorption analysis and transmission/reflection visible spectroscopy. *Anal. Chim. Acta* **262**, 269–275 (1992).
- Zhu, J. et al. Solvothermally controllable synthesis of anatase TiO_2 nanocrystals with dominant {001} facets and enhanced photocatalytic activity. *Cryst. Eng. Commun.* **12**, 2219–2224 (2010).
- Wang, J., Zhang, P., Li, X., Zhu, J. & Li, H. Synchronical pollutant degradation and H_2 production on a Ti^{3+} -doped TiO_2 visible photocatalyst with dominant {001} facets. *Appl. Catal. B: Environ.* **134**, 198–204 (2013).
- Liu, X., Dong, G., Li, S., Lu, G. & Bi, Y. Direct observation of charge separation on anatase TiO_2 crystals with selectively etched {001} facets. *J. Am. Chem. Soc.* **138**, 2917–2920 (2016).
- Xu, H., Ouyang, S., Li, P., Kako, T. & Ye, J. High-active anatase TiO_2 nanosheets exposed with 95% {100} facets toward efficient H_2 evolution and CO_2 photoreduction. *ACS Appl. Mater. Interfaces* **5**, 1348–1354 (2013).
- Tian, F., Zhang, Y., Zhang, J. & Pan, C. Raman Spectroscopy: A new approach to measure the percentage of anatase TiO_2 exposed {001} facets. *J. Phys. Chem. C* **116**, 7515–7519 (2012).
- Jun, Y. et al. surfactant-assisted elimination of a high energy facet as a means of controlling the shapes of TiO_2 nanocrystals. *J. Am. Chem. Soc.* **125**, 15981–15985 (2003).

30. Wu, N. et al. Shape-enhanced photocatalytic activity of single-crystalline anatase TiO₂ (101) nanobelts. *J. Am. Chem. Soc.* **132**, 6679–6685 (2010).
31. Yang, Q. et al. Do zinc dendrites exist in neutral zinc batteries: a developed electrohealing strategy to in situ rescue in-service batteries. *Adv. Mater.* **31**, 1903778 (2019).
32. Zhang, Q. et al. A facile annealing strategy for achieving in situ controllable Cu₂O nanoparticle decorated copper foil as a current collector for stable lithium metal anodes. *J. Mater. Chem. A* **6**, 18444–18448 (2018).
33. Zhang, C. et al. A ZnCl₂ water-in-salt electrolyte for a reversible Zn metal anode. *Chem. Commun.* **54**, 14097–14099 (2018).
34. Xie, X. et al. Manipulating the ion-transfer kinetics and interface stability for high-performance zinc metal anodes. *Energy Environ. Sci.* **13**, 503–510 (2020).
35. Zuo, T. et al. Graphitized carbon fibers as multifunctional 3D current collectors for high areal capacity Li anodes. *Adv. Mater.* **29**, 1700389 (2017).

Acknowledgements

This research was financially supported by the National Nature Science Foundation of China (No. 21975289), Hunan Provincial Research and Development Plan in Key Areas (2019GK2033) and Hunan Provincial Science and Technology Plan Project of China (No. 2017TP1001 and No. 2018RS3009).

Author contributions

H.W. designed the experiment and participated in the analysis of results and in discussing and writing the paper. Q.Z. participated in the experimental design, synthesized the samples, carried out the characterizations and wrote the manuscript. Y.T. provided valuable advice and participated in helpful discussions. X.H. and D.S. analyzed the data and edited the paper. X.J. participated in discussions on the paper. J.L. and Q.W. helped to characterize the materials. All authors have read and approved the final paper.

Competing interests

The authors declare no competing interests.

Additional information

Supplementary information is available for this paper at <https://doi.org/10.1038/s41467-020-17752-x>.

Correspondence and requests for materials should be addressed to H.W.

Peer review information *Nature Communications* thanks Seung-Tae Hong, and the other, anonymous, reviewer(s) for their contribution to the peer review of this work.

Reprints and permission information is available at <http://www.nature.com/reprints>

Publisher's note Springer Nature remains neutral with regard to jurisdictional claims in published maps and institutional affiliations.



Open Access This article is licensed under a Creative Commons Attribution 4.0 International License, which permits use, sharing, adaptation, distribution and reproduction in any medium or format, as long as you give appropriate credit to the original author(s) and the source, provide a link to the Creative Commons license, and indicate if changes were made. The images or other third party material in this article are included in the article's Creative Commons license, unless indicated otherwise in a credit line to the material. If material is not included in the article's Creative Commons license and your intended use is not permitted by statutory regulation or exceeds the permitted use, you will need to obtain permission directly from the copyright holder. To view a copy of this license, visit <http://creativecommons.org/licenses/by/4.0/>.

© The Author(s) 2020